Cosmic-ray transport and gamma-ray emission in M31

Audrey Do,[1] Matthew Duong,[1] Alex McDaniel,[2,*] Collin O'Connor,[1] Stefano Profumo,[1,3,†] Justine Rafael,[1] Connor Sweeney,[1] and Washington Vera III[1]

[1]*Department of Physics, University of California, Santa Cruz, California 95064, USA*
[2]*Department of Physics and Astronomy, Kinard Lab of Physics, Clemson, South Carolina 29634-0978, USA*
[3]*Santa Cruz Institute for Particle Physics, Santa Cruz, California 95064, USA*

(Received 18 May 2021; accepted 9 November 2021; published 8 December 2021)

We study the possibility that an extended cosmic-ray leptonic and/or hadronic halo is at the origin of the large-scale gamma-ray emission detected from the Andromeda galaxy (M31). We consider a broad ensemble of nonhomogeneous diffusion scenarios and of cosmic-ray injection sources. We find that cosmic-ray electrons and protons could be, and very likely are, responsible for part, or all, of the gamma-ray emission from M31, including out to more than 100 kpc from the center of the galaxy. We also simulate possible emission from pulsars in M31 and consider the effect of regions of highly inefficient diffusion around cosmic-ray acceleration sites, as suggested by recent TeV halo observations with Cherenkov telescopes.

DOI: 10.1103/PhysRevD.104.123016

I. INTRODUCTION

As the nearest large spiral galaxy to the Milky Way (MW), the Andromeda galaxy (M31) has been the subject of intense observational scrutiny, including recent detections at gamma-ray energies. While early gamma-ray telescopes were able to only set upper limits on the gamma-ray signal, the Fermi Large Area Telescope (LAT) [1] was the first instrument to obtain a significant positive detection [2]. The LAT detection was found to be compatible both with a point source and with an extended source emission tracing an infrared map at 100 μm intended to indicate star-forming regions, with the extended emission preferred nonsignificantly at the confidence level of 1.8σ [2]. Subsequent studies of LAT data including longer exposure have added to the evidence for gamma-ray emission in M31, including the tentative, and controversial, detection of potential "bubblelike" features analogous to the Milky Way Fermi bubbles [3]. In a recent study, the Fermi-LAT Collaboration reported a 10σ detection of M31 with a strong detection of spatially extended emission out to $\sim$5 kpc at the 4σ significance level [4].

The nature and origin of the emission from the central regions of M31 remain somewhat controversial. On the one hand, M31's observed gamma-ray luminosity does not significantly deviate from the expectation from the known scaling relationship between infrared and gamma-ray luminosity [5,6]; this, in turn, would hint at cosmic rays, accelerated in supernova explosions, as the physical counterpart to the observed emission. This possibility was quantitatively explored in [7], which found, however, that the required input power from supernova explosion would imply, in the case of a leptonic or hadronic or even of a mixed scenario, a supernova rate around two orders of magnitude larger than expected. References [8,9] explored, instead, a dark matter annihilation scenario, where gamma rays originate as a result of the pair-annihilation of dark matter particles. This possibility was recently also considered in [10]. While, in principle, consistent with the so-called, controversial, "Galactic Center Excess" in the Milky Way [11], and marginally in tension with the non-observation of gamma-ray emission from local dwarf galaxies by Fermi-LAT [12,13], this is an intriguing possibility. Finally, unresolved emission from point sources such as millisecond pulsars or other compact objects, which has been considered in Fragione *et al.* [14] as well as in Eckner *et al.* [15], remains an unavoidable component of the observed signal, albeit with uncertain relative importance.

Other recent observations of gamma-ray emission in M31 have searched for emission at large radii in the outer halo of the galaxy. As part of a detailed study of the gamma-ray emission in M31 using roughly 8 years of Fermi-LAT data in a 60° region of interest centered at $(l, b) = (121.17°, -21.57°)$, Karwin *et al.* [16] reports evidence for an extended gamma-ray excess separate from the Milky Way foreground. This purported emission extends out to roughly 100–200 kpc above the plane of the galaxy, although the authors acknowledge that the emission from the "far outer halo" (at angles from M31's

*armcdan@clemson.edu
†profumo@ucsc.edu

center $8.5° < r < 21°$) is likely related to mismodeling of the significant foreground emission from the Milky Way and thus less robust than the emission from the "spherical halo" region at angles between $0.4° < r < 8.5°$ and than the robustly detected inner galaxy emission at $r < 0.4°$. Karwin *et al.* [16], while not ruling it out, argues against an extended cosmic-ray halo [17,18] based on the radial extent, spectral shape, and intensity of the observed large-radii signal. However, as we argue below, the radial extent and intensity depend critically on assumptions on cosmic-ray diffusion outside the Galactic plane and in the halo, and the spectral shape is strongly affected by foreground Galactic emission and from the intrinsic weakness and limited statistics of the signal.

In this study, we study cosmic-ray electron and proton transport in M31 under a variety of assumptions on the nature of diffusion within and beyond the traditional cylindrical "diffusion box", used in Milky Way cosmic-ray studies, around M31's galactic plane. We note that recent studies (see, e.g., [19,20]) advocate for the importance of cosmic-ray streaming in the energy range of interest here and for a hadronic gamma-ray production model; specifically, studies indicate that streaming should be included at least at certain scales to describe cosmic-ray outflow [21]. Recent gamma-ray spectroscopy studies in the Milky Way also provide evidence of efficient streaming of cosmic rays that can produce gamma-rays away from the Galactic disk [22]. Here, for simplicity, we assume that diffusion dominates cosmic-ray transport *overall* in the large ~100 kpc radius region of interest we consider and leave the study of the possible effect of streaming to a future investigation. We similarly neglect the possible anisotropy in the diffusion coefficient; including this additional possible effect would make our models increasingly hard to constrain and less predictive.

Since we relax the simplifying assumption of homogeneity for the diffusion coefficient, we solve the transport equation via a stochastic approach in the standard way (namely, turning the Fokker-Planck partial differential equation describing cosmic-ray transport into a stochastic differential equation solved by means of a Monte Carlo method). We consider both a sharp discontinuity and a gradual transition from the inside to the outside of the inner diffusion region; in addition, we also consider a model, that is becoming increasingly well motivated by observations of TeV halos [23], where diffusion within the sites of cosmic-ray acceleration is inefficient. Finally, we also consider a variety of possible injection sites for the cosmic rays.

Cosmic-ray electrons and protons both produce gamma rays as they propagate through the Galaxy. However, while electrons radiate highly efficiently and lose energy quickly, protons' energy losses are significantly less efficient, with timescales much longer than those associated with propagation. At the gamma-ray energies of interest, and in the outer regions we are concerned with, cosmic-ray electron emission proceeds through inverse-Compton scattering, primarily by up-scattering photons in the cosmic microwave background (CMB). Cosmic-ray protons instead produce gamma rays as a result of inelastic collisions with the interstellar and circumgalactic medium, producing neutral pions eventually decaying to gamma-ray pairs.

In this study, we also reassess the contribution of millisecond pulsars and of younger pulsars to the gamma-ray emission, making use of dedicated pulsar population synthesis modeling and of observationally motivated predictions for gamma-ray emission from pulsars.

Our results indicate that it is quite plausible that (i) most of the spherical halo gamma-ray emissions originate from a cosmic-ray halo possibly extending out to M31's virial radius and well beyond the galactic disk. We find that this interpretation is (ii) possible both within hadronic and leptonic cosmic-ray scenarios, albeit in the latter case only a fraction of the spherical-halo gamma-ray emission can be explained. Finally, we find that (iii) the inner-galaxy emission is most likely a combination of pulsar gamma-ray emission and of hadronic and leptonic cosmic-ray-induced gamma rays, somewhat attenuating the tension with the expected supernova rate found in [7].

The remainder of this study is structured as follows: in Sec. II, we outline our approach to solving the relevant transport equation and give details about the diffusion and cosmic-ray models we consider. Sections III and IV detail our results on cosmic-ray driven gamma-ray emission and on pulsar gamma-ray emission, respectively; finally, Sec. V presents a final discussion of our results and our conclusions.

II. SOLUTION TO THE TRANSPORT EQUATION AND DIFFUSION MODELS

The transport of cosmic rays on galactic scales, describing the particles' flux and energy spectrum $n(\vec{x}, \vec{p}, t)$, with $\vec{x}$ position and $\vec{p}$ momentum, is customarily described through diffusive processes in phase space via equations with a structure of the type [24]

$$\frac{\partial n}{\partial t} + \vec{u} \cdot \nabla n = \nabla \cdot (\hat{\kappa} \nabla n) + \frac{1}{p^2} \frac{\partial}{\partial p} \left(p^2 \kappa_{pp} \frac{\partial n}{\partial p} \right) + \frac{1}{3} (\nabla \cdot \vec{u}) \frac{\partial n}{\partial \ln p} + S(\vec{x}, p, t). \quad (1)$$

In the equation above, $\vec{u}$ is the advection speed, $\hat{\kappa}$ the spatial diffusion tensor, $p = |\vec{p}|$, κ_{pp} the momentum-space diffusion coefficient which effectively describes reacceleration, and $S(\vec{x}, p, t)$ describes the cosmic-ray sources.

An important consideration when discussing cosmic-ray (CR) transport in M31 is the role of diffusive effects versus possible contributions from winds. Typically, the star formation activity in a galaxy can be used as an indicator of the presence of a CR driving wind [25–27]. In [28], Hα observations of spiral galaxies were used to estimate a

lower limit on wind driven outflows at 3.2×10^{40} ergs s^{-1} kpc^{-2} in terms of the star formation rate (SFR)/per unit area which gives a total SFR of $\sim 0.58\ M_\odot\ \mathrm{yr}^{-1}$ for a radius of 20 kpc. In comparison, recent observations of M31 over the same scale find global SFR rates of ~ 0.25–$0.3\ M_\odot\ \mathrm{yr}^{-1}$ [29,30] (though some other studies have found slightly higher total SFR up to $\sim 0.4\ M_\odot\ \mathrm{yr}^{-1}$ [31]). This suggests that the role of winds in producing the halo in M31 may be a subdominant process and motivates our interest in focusing on the diffusion process. This is in line with previous studies of M31 and other galaxies [32,33], as well as recent simulations [34], where the role of winds in CR propagation is found to be of lesser impact than diffusion.

In the context of CR transport, the diffusion equation has been solved through a variety of methods. In Colafrancesco *et al.* [35,36], a Green's function method, with image "charges" suitably accounting for the boundary conditions of the problem, was developed and employed to solve for the steady-state solution to a diffusion problem with spherical symmetry, for arbitrary injection spectra, but with a spatially constant energy loss term and diffusion coefficient [see also [37]]. The method was generalized in [8] for the calculation of the radio and inverse-Compton emission, with the possibility to also include a spatially dependent magnetic field and target radiation field energy density.

An alternate approach is to solve for the differential equation on a lattice by discretizing the problem in a standard fashion. This method is employed by popular codes that solve for the diffusion problem in cylindrical coordinates such as GALPROP [38] or DRAGON [39,40]. While this method can, in principle, be adapted to different geometries and to different assumptions on the spatial dependence of the various transport coefficients, the method is not easily adapted to complex diffusion setups such as the ones we are interested in here.

Finally, using the well-known connection between the Fokker-Planck equation and Stochastic differential equations, other codes model CR transport by means of stochastic processes, see, for example, the CRPropa code [41,42]. Here, we utilize precisely this approach, as it is the most flexible to study largely inhomogeneous diffusion setups and complex CR injection morphologies. We refer the reader to classic literature on the equivalence between Fokker-Planck partial differential equations and stochastic differential equations, see, e.g., [43].

We model diffusion as a stochastic process in space (we model energy losses separately and neglect reacceleration and streaming). We assume diffusion to be isotropic; thus, each pseudoparticle's step is taken to occur in a random direction in space. The step size is taken to correspond to the mean free path λ, which for a diffusive process in three dimensions is $\lambda \simeq 3D/v$, with D the (energy-dependent) diffusion coefficient at the particle's location and v the pseudoparticle velocity; for instance, for typical values of $D \sim 3 \times 10^{28}\ \mathrm{cm}^2/s$ and $v \simeq c$, we get $\lambda \simeq 1$ pc. Since the diffusion coefficient is taken to be a function of energy so is the corresponding mean free path. To reduce the computational complexity of our simulations, we occasionally needed to resort to extrapolations of the results of simulations with larger step sizes. The extrapolation procedure involves running several simulations with the same parameters, except with different step sizes. At each step size, there is a density of particles for a given radius. The densities are extrapolated as a function of step size, and a best fit line is produced from the results. We then extrapolate the density to a step size of .002 using the best fit line. A visual of this procedure is shown in Fig. 1, left.

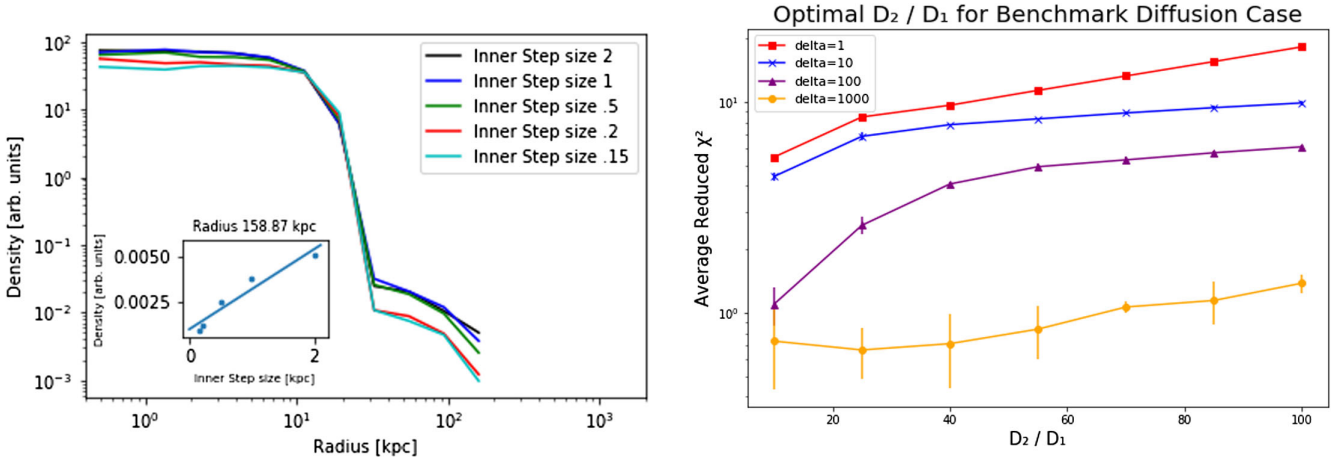

FIG. 1. Left: illustration of an extrapolation procedure used in some of our simulations. The inner step size refers to the step size within the diffusion region. This image represents the CRP1 diffusion setup. Right: averaged χ^2 for a fit to the observed gamma-ray emission morphology from cosmic-ray protons with an ensemble of simulation at various values of the width of the transition region δ and of the ratio D_2/D_1. The optimal choice corresponds to $D_2/D_1 = 25$ and $\delta = 1000$ kpc.

To model the CR spatial distribution in steady state (the case of interest here, since we assume all injection sources to be in steady state), we run our simulations with a limited number of pseudoparticles and assess the CR residence timescale τ for pseudoparticle loss outside the region of interest (which is typically taken to be 200 kpc, the same region of interest used in [16], and around 2/3 of M31's virial radius) by fitting, after an initial transient, for the exponential decay behavior of the number $N(t)$ of pseudoparticles still within the diffusion region versus the total initial number of particles $N(t=0)=N_0$,

$$N(t) \simeq N_0 \exp(-t/\tau). \tag{2}$$

In practice, we fit the exponential form to the interval $0.1 < N(t)/N_0 < 0.9$ to prevent both fitting for the initial transient corresponding to the drift to the boundary of the diffusion region and for the noisy tail of the distribution at the end of the simulation. Once the residence timescale τ is found, we run extensive simulations with a large number of pseudoparticles (on the order from 10^6 to 10^8) for a time $t=\tau$.

We validated the procedure outlined above and the code by comparing our results with a simplified version of the diffusion equation's Green function, which solves

$$\frac{\partial n}{\partial t} = \nabla \cdot (\hat{\kappa} \nabla n) + \delta(\vec{r})\delta(t) \tag{3}$$

and which reads

$$n(r_i, t) = \frac{\exp\left(-\frac{r_i^2}{4\kappa_{ii}t}\right)}{(4\pi\kappa_{ii}t)^{d/2}}, \tag{4}$$

with d the dimension and κ_{ii} the diffusion coefficient in the direction r_i. We cross-checked our code for $d=1,\ldots,3$ and for isotropic and nonisotropic diffusion tensors. We completely developed the code we employed in-house.

We neglect energy losses for the case of cosmic-ray protons, while in the case of cosmic-ray electrons we assume the standard quadratic dependence on energy for energy losses for high-energy electrons,

$$\frac{dE}{dt} \simeq -b_0 E^2, \tag{5}$$

with $b_0 \sim 10^{-16}\ \mathrm{GeV}^{-1}\,\mathrm{sec}^{-1}$ [35]. Notice that here we neglect effects related to the transition of the electron energy losses from the Thomson to the Klein-Nishina regime (see Ref. [44] for a recent evaluation of the impact of this approximation); we leave it to future work to implement the full Klein-Nishina energy loss formula. One can integrate the equation above by separation of variables between an initial and a final time/energy to get (for initial time $t=0$)

$$-\frac{1}{E_f} + \frac{1}{E_i} = -b_0 \delta t = -b_0 \delta x / c, \tag{6}$$

where in the last equation we assumed that the propagation step between collisions δx has length $\delta x = c\delta t$ because the electrons are ultrarelativistic. Solving for E_f, one finds

$$E_f = \frac{E_i}{1 + (\frac{b_0}{c})\delta x E_i}. \tag{7}$$

Expressing x in kpc and E_i in GeV, the multiplicative constant gives

$$E_f = \frac{E_i}{1 + 10^{-5}\,\frac{\delta x}{\mathrm{kpc}}\,\frac{E_i}{\mathrm{GeV}}}. \tag{8}$$

Thus, in the case of the electrons, we run simulations that track not only position but also energy. We assume an injection spectrum inspired by Fermi second-order acceleration, $dN/dE \sim 1/E^2$, and spawn electrons with energy in proportion to that spectrum; we then track both where the final positions of the electrons are and which energy they have, with the proviso that for every step where the electron has moved by a distance x the energy is reduced according to Eq. (7) above.

Notice that while we diffuse electrons in the same way as protons, i.e., simulating diffusion via a stochastic processed as described above, the relevant timescale for the simulation in this case is the *energy-loss* timescale rather than the diffusion of the particles outside the diffusive region of interest. The energy-loss timescale is defined by the number of steps it takes particles to fall below an energy such that emission of gamma rays in the energy range to which the Fermi-LAT is sensitive to is no longer viable. Since we are interested here primarily in emission far away from the stellar population in M31 (and, in particular, distances typically larger than the size of the stellar disk in M31), the main photon field we are concerned with is the cosmic microwave background (the inverse-Compton emission scales with the energy density in a given radiation field, and in the spherical halo, this is dominated by the CMB). The average energy of a CMB photon is $E_\gamma \simeq 6.4 \times 10^{-4}$ eV; the typical energy of the up-scattered photon is $E_f \sim \gamma_e^2 E_\gamma$, where γ_e is the Lorentz factor of the incoming electron. Requiring $E_f \gtrsim 0.1$ GeV, which is at the lowest energy detectable by the LAT, we get that $\gamma_e = E_e/m_e \gtrsim \sqrt{E_f/E_\gamma} \simeq 4 \times 10^5$, thus $E_e^{\mathrm{min}} \simeq 200$ GeV. Notice that the energy dependence of the diffusion coefficient is quite critical in the case of high-energy electrons, $D(E) = D_0 (E/\mathrm{GeV})^\xi$, and adopt the canonical Kolmogorov value of $\xi = 0.3$. This energy dependence of the diffusion coefficient is well supported by a variety of studies, including direct local cosmic-ray observations [45] and complex CR propagation modeling and simulations

[34,46,47], along with observations of external galaxies [32,33]. Radio observations in M31 [32] specifically have also shown to be consistent with an energy-dependent diffusion coefficient lending further credence to the suitability of its application in this study.

We can estimate the average path length λ_e the electrons take to lose their initial energy E_i from Eq. (7) above; being a diffusive process, we first calculate the time $T_{i\to f}$ for the electrons to lose energy from E_i to E_f,

$$T_{i\to f} = \frac{1}{b_0}\left(\frac{1}{E_f} - \frac{1}{E_i}\right) \simeq 10^{16}\ \frac{\mathrm{GeV}}{E_f}\ \mathrm{sec}\,. \tag{9}$$

The typical distance traveled by an electron from its injection point is then given by

$$\lambda_e \simeq \sqrt{D_0(\bar{E}/\mathrm{GeV})^{\xi} T_{i\to f}} \sim 5.8\ \mathrm{kpc}\left(\frac{E_f}{\mathrm{GeV}}\right)^{-0.35} \approx 0.9\ \mathrm{kpc}, \tag{10}$$

where in the last equation we assumed $E_f \simeq 200$ GeV. Thus, electrons contributing IC emission off of CMB are not expected to diffuse further than approximately 1 kpc from the source location. Our simulations are found to be consistent with the simple estimate above.

While in the case of electrons up-scattering CMB photons, there is a one-to-one correspondence between the final electron locations and the gamma-ray emission along a given line of sightl in the case of protons, the structure of the interstellar and circumstellar target gas density is crucial, as the gamma-ray emissivity is proportional to the line-of-sight integral of the product of the cosmic-ray proton density and the target gas density. Given the lack of detailed information about the gas density along the line of sight especially between the MW and M31 centers, we choose to adopt the results of the simulations in [48]. Specifically, we utilize their results on the gas density along the line of sight between M31 and the MW (thick black line in Fig. 16), up to a distance of approximately 30 kpc from M31; at that point, we match the gas density in their simulation results for the gaseous halo of M31, Fig. 5, left panel. Finally, we use the results of the simulations in [49], their Fig. 1, summing upon all components, in the innermost 1.5 kpc.

In producing the gamma-ray morphology plots, we simply count the number of pseudoparticles corresponding to cosmic-ray electrons, given the homogeneity of the background radiation field. In the case of cosmic-ray protons, we instead weigh each pseudoparticle with the corresponding target gas density at its location and then integrate (i.e., sum) along the given line of sight.

In order to compare our results with observations, we digitized the map corresponding to the tentative signal (i.e., residual) intensity map in [16], Fig. 34, top left, using the numpy, matplotlib, and OpenCv libraries in Python to digitally input the image and the associated color bar, which was then converted from RGB values back into physical values using the nearest color index of the color bar. This was then scaled down to the source's original 20×20 pixel resolution. We note that the source image contained overlays for spatial reference, which resulted in artifacts upon digitizing and rescaling; in order to resolve this, pixels were manually corrected by sampling the nearest unaffected pixels from the full-scale digitized image.

III. RESULTS

In this analysis, we test the impact of both the source morphology and the diffusion setup on the gamma-ray emission from (i) inelastic collisions of cosmic-ray protons with the inter-stellar medium and (ii) inverse-Compton emission of high-energy cosmic-ray electrons off of CMB photons, using the simulation techniques described in the previous section. We note that while in the galactic plane other photon fields than the CMB have comparable energy density to CMB photons, in the region of interest we are concerned with CMB photons dominating on average by 1 to 2 orders of magnitude the background photon energy density. We thus neglect other photon fields in our study.

As far as the source morphology is concerned, we entertain three scenarios:

(1) Cosmic rays are produced near the central region of M31; this scenario assumes that the main acceleration mechanism for cosmic rays in M31 is physics associated with the innermost region of the galaxy, such as, for instance, accretion around, and jets emanating from, the central supermassive black hole of M31 (see Ref. [3] and the results of extended *Chandra* X-ray observations of M31*, indicating outburst phases and significant flux variations, similar to those observed for Sgr A* [50]).

(2) Cosmic rays are produced in star-forming regions; this possibility physically relies on the notion that the main cosmic-ray acceleration sites are likely supernova shocks, whose locations trace star-forming regions. Observationally and theoretically, this possibility was explored in [51,52] and in [53], which found that a significant fraction of cosmic rays in the Milky Way are likely injected from star-forming regions. We use as a tracer of star-forming regions in M31 the IR emission map from [54].

(3) Finally, we use the `PrsPopPy` code ([55]) to produce a synthetic population of pulsars (see Sec. IV for details on the population synthesis procedure we adopt) as a proxy for a scenario where cosmic-ray electrons and positrons are produced in the magnetosphere of rotating neutron stars [see, e.g., [56,57]].

We also entertain a variety of diffusion models, taking advantage of the flexibility provided by the stochastic

solution to the diffusion equation. In particular, we assume the following:

(a) A traditional "leaky box" diffusion scenario (hereafter referred to as our "benchmark" model) inspired by similar setups for the Milky Way that successfully reproduce the measured abundance of cosmic-ray species [see, e.g., [38–40]]. Here, we assume that cosmic rays diffuse primarily inside a cylindrical diffusion region of radius 20 kpc and half-height 10 kpc (we have also considered variations of these parameters, with marginal impact on our results described below), effectively free-streaming outside the diffusion region; we model this latter effect by a sudden, steplike jump by a factor of 100 in the diffusion coefficient outside the cylindrical box.

(b) A "constant" diffusion scenario, where cosmic rays diffuse in an isotropic and homogeneous medium with a constant diffusion coefficient. Albeit physically unrealistic, this scenario aims at assuming that the circumgalactic medium in the Local Group continues to support cosmic-ray diffusion well outside M31 and the Milky Way and out to much larger radii than the galaxies' sizes.

(c) A "gradual" spatially dependent diffusion coefficient defined so that the diffusion coefficient inside a cylindrical box of height z_t and radius r_t is D_1 and, after a transition region of size δ, it asymptotes to an outer value D_2. The distance of a point (r, z) in cylindrical coordinates from the diffusion box is

$$\mathrm{dist}(r,z) = \sqrt{(r - \min[r, r_t])^2 + (z - \min[z, z_t])^2}. \quad (11)$$

The diffusion coefficient at a point of cylindrical coordinates (r, z) is then calculated as

$$D(r,z) = D_1 + (D_2 - D_1)\frac{\mathrm{ArcTan}[\mathrm{dist}(r,z)/\delta]}{\pi/2}. \quad (12)$$

We searched for the values of D_2/D_1 and δ producing the gamma-ray emission morphology most closely resembling (based quantitatively on a pixel-by-pixel χ^2 procedure) the diffuse gamma-ray emission measured in the inner halo and spherical halo of M31 [16]. For this calculation, we utilized the gamma-ray emission from cosmic-ray protons, with the procedure explained above. The χ^2 was computed by comparing the predicted and measured emission pixel by pixel in a 20×20 pixel region covering the entire region of interest (with a radius of 27 kpc, corresponding to an approximate angular scale of four degrees), after normalizing both maps to the same average emission. We show in Fig. 1, right, the results for the χ^2 for different values of δ and D_2/D_1. For every combination of D_2/D_1 and δ, we ran a set of ten independent simulations, with the inferred standard deviation shown in the figure. Our results indicate a preference for *large* values of δ, implying, in turn, a preference for a mild "gradient" in transitioning to the larger outer value of the diffusion coefficient. Similarly, we observe a preference for smaller ratios of the outer to inner diffusion coefficient. However, for large $\delta \sim 1$ Mpc, we find that ratios $5 \lesssim D_2/D_1 \lesssim 50$ give equally good fits to the observed morphology. While there is no strong statistical preference, we adopted as our benchmark choice the lowest χ^2 central value which corresponded to $D_2/D_1 = 25$. We show in Fig. 2 with an isolevel contour plot in the left and with a three-dimensional rendering of a 100×100 kpc region on the right the resulting

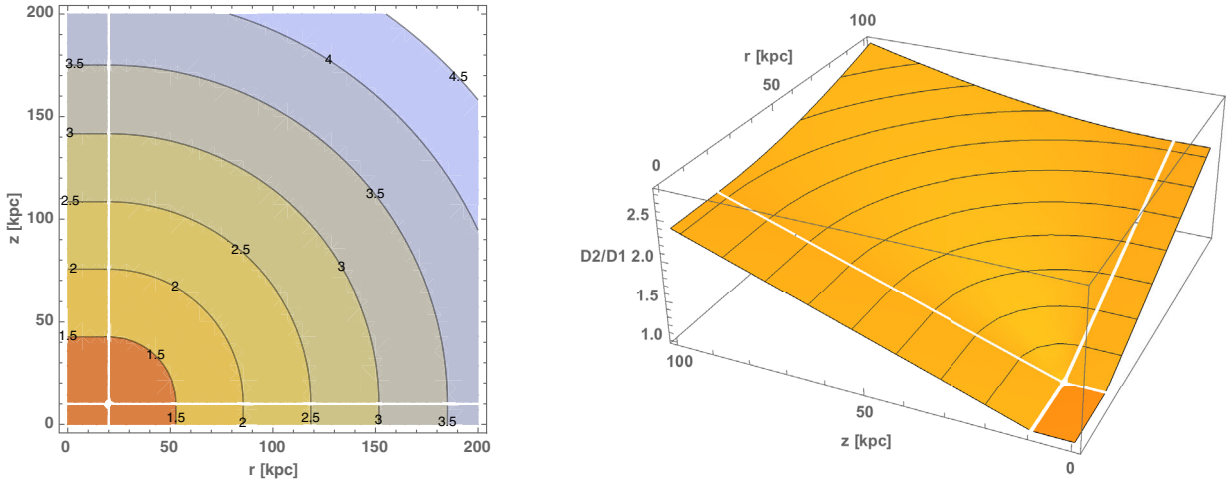

FIG. 2. Spatially varying diffusion coefficient, with the functional form in Eq. (12) and $D_2/D_1 = 25$ and $\delta = 1000$ kpc. The left panel shows curves of constant D_2/D_1 on the (r, z) plane of cylindrical coordinates across the entire region of interest, while the right panel shows a three dimensional plot of the same quantity, on the same plane. The inner diffusion region, with constant $D = D_1$, is bordered by white lines.

diffusion coefficient (normalized to the value inside the inner diffusion box) in cylindrical coordinates (r, z), with parameters corresponding to the optimal choices $D_2/D_1 = 25$ and $\delta = 1000$ kpc.

(d) As a second example of a spatially varying diffusion coefficient, we utilize a model (which we dub "Swiss cheese" diffusion coefficient) where inside the diffusion region there exist spherical subregions of inefficient cosmic-ray transport associated with the turbulent medium inside pulsar wind nebulae (PWNe). This scenario reflects the recent findings of [23] that high-energy cosmic-ray electrons diffuse much less efficiently (around a factor 100 smaller effective diffusion coefficient) inside PWNe than outside. Following [58], we use the model of [59] to relate the pulsar age to the radial size of the corresponding PWN, and we assume a sudden transition to a diffusion coefficient $D_0/100$ inside the PWN; outside the cylindrical box, we assume, as for the benchmark model, a large diffusion coefficient $100 \times D_0$.

We employ slightly different sets of source distribution and diffusion models for cosmic-ray electrons (CRE) and protons (CRP), based on different expected injection sources (protons are not thought to be produced by pulsars' magnetospheres). We describe below our choices and results.

A. Cosmic-ray electrons

Here, we present results for gamma rays from inverse-Compton (IC) up-scattering of CMB photons by high-energy cosmic ray electrons. We consider six different cases:

CRE1: Benchmark diffusion scenario (a), with CRE injected at the very center of M31, i.e., scenario (i).
CRE2: Benchmark diffusion scenario (a), with CRE injected in star-forming regions, i.e., scenario (ii).
CRE3: Benchmark diffusion scenario (a), with CRE injected at the location of mature synthetic pulsar locations, i.e., scenario (iii).
CRE4: Constant diffusion scenario (b), with CRE injected at the very center of M31, i.e., scenario (i).
CRE5: Gradual diffusion scenario (c), with $D_2/D_1 = 25$ and $\delta = 1,000$ kpc, with CRE injected at the very center of M31, i.e., scenario (i).
CRE6: "Swiss cheese" diffusion scenario (d), with CRE injected at the location of mature synthetic pulsar locations, i.e., scenario (iii).

Figure 3 shows the emission morphology from IC of CMB photons by CRE. We notice that virtually in all cases the emission is mostly circumscribed to the inner regions of M31, albeit with different morphologies for the different assumptions on diffusion and source location. The radially averaged intensity profiles of the six cases is shown in Fig. 4. First, we note that CRE1 and CRE5 are very similar, indicating that the transport conditions beyond the inner regions play a relatively mild role. In these cases, there is also very marginal emission in the spherical halo region. CRE2 and CRE3 also look remarkably similar, as is somewhat expected since in both cases the CR injection sites trace star formation. In CRE2 via the IR emission map, we utilized as a proxy for the star formation rate, and in CRE3 via the synthetic pulsar population model, we constructed (described in detail in the following section). CRE2 and CRE3 exhibit a more extended morphology

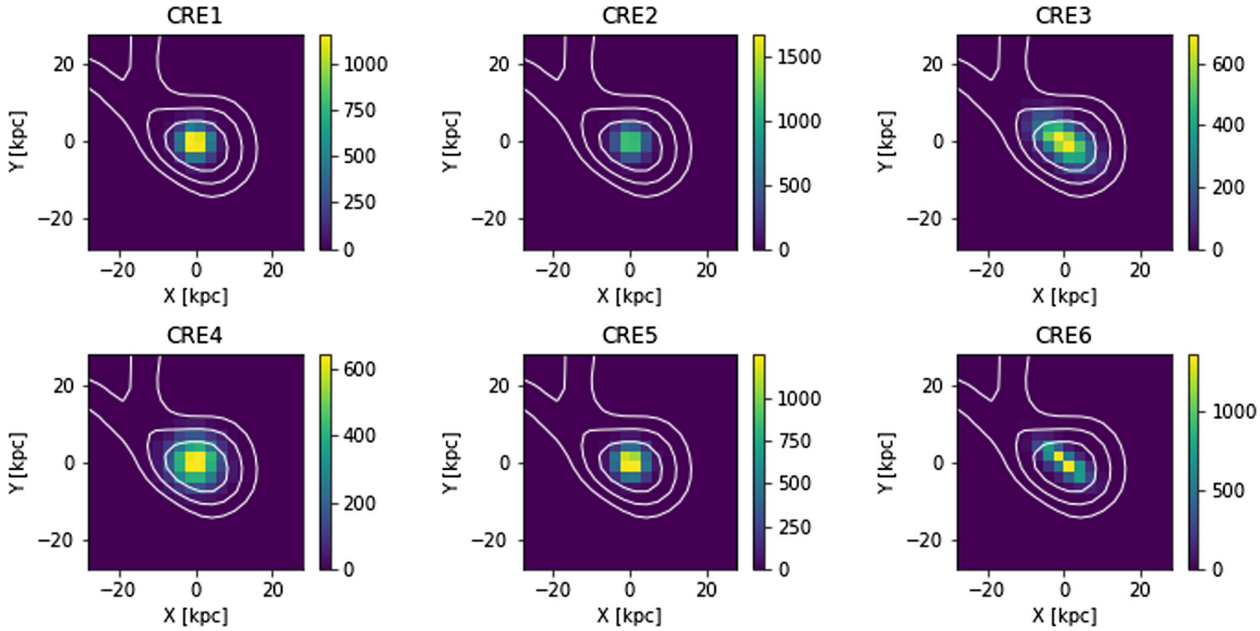

FIG. 3. Morphology of each of the six CRE cases. For each case, a contour plot of the observed gamma-ray emission from the Fermi-LAT observations [16] is mapped over the CRE configurations for comparison.

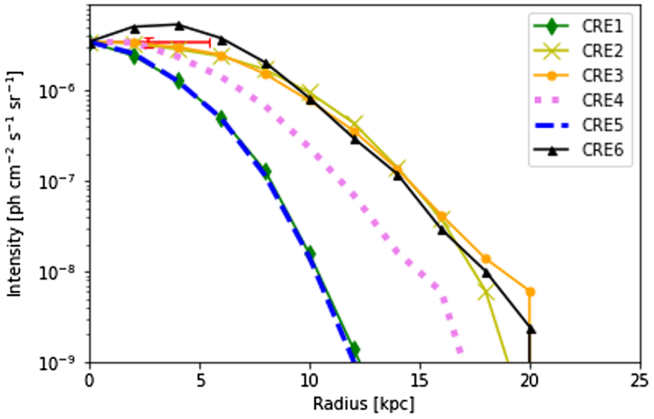

FIG. 4. Radial intensity profile for cosmic-ray electron simulations for the six diffusion and injection source profile combinations discussed in the text.

compared to CRE1 and CRE5 and are found to contribute somewhat to the emission in the spherical halo region, which is around 5×10^{-8} ph cm^{-2} s^{-1} sr^{-1}, out to around 15 kpc. Finally, CRE6 is the model that has the most pronounced emission in the innermost few kpc, driven by CR electrons being "trapped" in bubbles of inefficient transport associated with PWNe.

The results of our simulations demonstrate the feasibility of diffusion-dominated CRE propagation out to large radii in M31. This can have important implications on our understanding of faint halo emission in galaxies and at other wavelengths. In particular, ARCADE-2 results have reported an excess of radio emission of undetermined origin [60–63], which has been seen in other radio studies as well [64]. If, as our results suggest, CRE propagating through primarily diffusive processes are able to produce emissions at large scale around their host galaxies, the resulting diffuse synchrotron emission may have a meaningful impact on the observed extragalactic radio background. However, production of synchrotron emission at larger radii would require not only the presence of CRE but also that there exists sufficient magnetic fields in order to produce synchrotron radio emission.

These results are also relevant to understanding the relation between the radio and far-infrared (FIR) emission in galaxies, which is strongly impacted by CRE propagation. The tight radio-FIR correlation has been extensively studied in external galaxies [65–67] including in particular M31 [32,68,69] and has been well established over a range of wavelengths and galaxy properties [25]. In radio-FIR studies of M31 (e.g., [32,69]), a critical parameter in understanding this correlation is the diffusion length scale which is found to be around ~1 kpc, in agreement with the values used in our simulations. As shown in our simulations, a diffusion driven CRE propagation model neglecting winds can produce emission from CRE out to large radii (e.g., CRE4 and CR5 in Fig. 4), consistent with the gamma-ray observations, while simultaneously remaining compatible with the diffusion parameters that characterize the FIR-radio correlation in M31. However the radio-FIR correlation still holds for galaxies where advection is expected to play an important role, for instance, M33 [32] or M82 [70,71]. In these instances, it may be possible that greater CRE injections are counteracted by shorter escape times due to the presence of the galactic winds [71–73]. Furthermore, regions of galaxies undergoing active star formation commonly host turbulent magnetic fields [74], and therefore, as the new, young CRE are injected into the galaxy, they synchrotron radiate near their initial injection site. This replenishment of young CRE is necessary in order to maintain the radio-FIR balance in these regions as the CRE rapidly loses energy in the turbulent magnetic fields [75,76]. For galaxies and regions that are not currently undergoing intense star formation activity (e.g., most of Andromeda), in order to follow the same radio-FIR trend, it is needed that the older CRE populations have time to diffuse and travel throughout the galaxy and its gaseous halo [76]. This is precisely the scenario depicted in our simulations of M31, and we in fact see that the gamma-ray observations are compatible with a population of older CRE that has diffused and traveled through the galaxy and out to large radii.

B. Cosmic-ray protons

In the case of protons, which are not produced in pulsars' magnetospheres, we consider a different set of cases (although, to ease the comparison with the CRE case, we follow a similar numbering convention), specifically:

CRP1: Benchmark diffusion scenario (a), with CRP injected at the very center of M31, i.e., scenario (i).
CRP2: Benchmark diffusion scenario (a), with CRP injected in star-forming regions, i.e., scenario (ii).
CRP4: Constant diffusion scenario (b), with CRP injected at the very center of M31, i.e., scenario (i).
CRP5: Inhomogeneous "gradual" diffusion scenario (c), with $D_2/D_1 = 25$ and $\delta = 1,000$ kpc, with CRP injected at the very center of M31, i.e., scenario (i).
CRP6′: "Swiss cheese" diffusion scenario (d), but with CRP injected in star-forming regions, i.e., scenario (ii).

As above, we show in two separate figures the results for the morphology of the innermost 25×25 kpc region in Fig. 5 and the radial intensity profile in Fig. 6. Our results indicate that CRP1, CRP2, and CRP6′ all exhibit a relatively similar morphology, likely due to the fact that in those cases the emission tracks quite closely the residence time, in turn related to the diffusion coefficient. Since protons diffuse for much longer times than electrons, the source injection site is less critical, and information thereof is asymptotically lost.

Larger values of the diffusion coefficient in the spherical halo and outer halo regions, as in CRP4 and CRP5, yields,

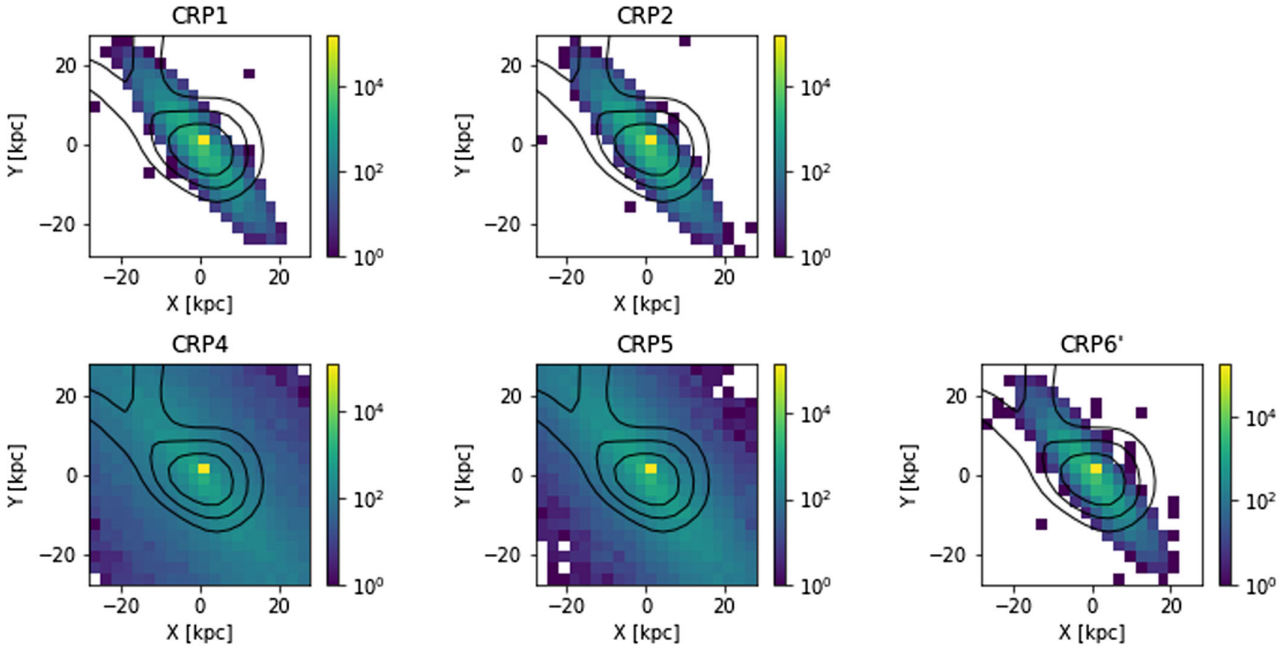

FIG. 5. Morphology of each of the five CRP cases. For each case, a contour plot of the observed gamma-ray emission from Fermi-LAT Karwin *et al.* [16] is mapped over the CRP configurations for comparison.

as expected, a much brighter emission at large radii; because CRP5 has a gradual ramp up to a larger diffusion coefficient, its relative brightness at large radii is lower than the constant diffusion coefficient case of CRP4. This is also clearly shown in the radial intensity profile of Fig. 6.

Our results for cosmic-ray protons indicate, as somewhat expected, that in order to support significant emission beyond the inner region, a comparatively small diffusion coefficient needs to be present in the outer regions of M31, as in CRP4 and CRP5. In either case, including when, as shown in Fig. 2, the diffusion coefficient is almost five times larger at the outskirts than around the inner M31 regions, the gamma-ray emission in the spherical halo and

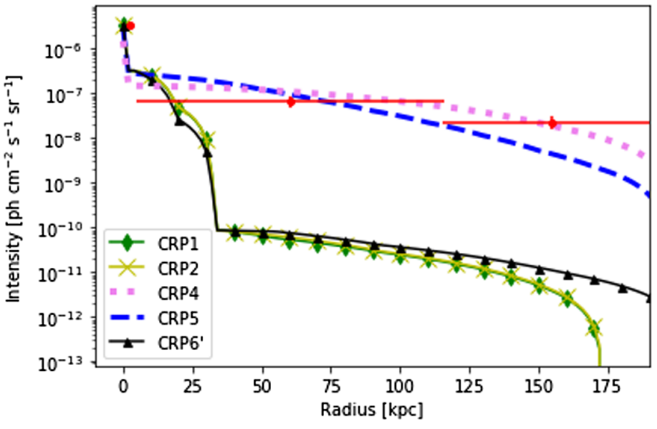

FIG. 6. Radial intensity profile for cosmic-ray proton simulations for the five diffusion and injection source profile combinations discussed in the text.

that in the inner region are quite accurately reproduced. Only a constant, suppressed diffusion coefficient would explain the outermost gamma-ray emission; in this case, the emission in the inner region would also additionally be self-consistently explained (see the pink dashed line in Fig. 6).

C. Spectral information

Ackermann *et al.* [4] find that the gamma-ray emission from M31 follows a power law with spectral index $\Gamma = 2.4 \pm 0.1$. Here, we study the implications of spectral information on a cosmic-ray electron or proton scenario.

The spectrum of gamma rays $dN/dE_\gamma \sim E^{-\Gamma_\gamma}$ from proton-proton inelastic collisions where the primary protons have a spectrum $dN/dE_p \sim E^{-\Gamma_p}$ depends on the assumed hadronization model [see, e.g., [77]]. For instance, in the so-called *Dermer's* model [78], $\Gamma_\gamma = \Gamma_p$, implying a proton spectral index $\Gamma_p \simeq 2.4$, somewhat harder than what is observed in the Milky Way, where $\Gamma_p \simeq 2.6$ [79]; in the *Fireball* model [80], similarly, the relation is $\Gamma_\gamma = (4/3)(\Gamma_p\text{-}1/2)$, implying $\Gamma_p = 2.3$. We note that differences in Γ_p could be related to different injection source spectra and/or a different energy dependence of the diffusion coefficient or both.

Spectral information in the case of cosmic-ray electrons is significantly blurred by a variety of circumstances, including the strongly energy-dependent diffusion, and the unknown spectra of the relevant background radiation up-scattered in inverse-Compton processes. However, in this case, it is possible with our setup to study the *morphology* of the predicted signal given an injection

spectrum. In the preceding section, we assumed that CRE featured a $\Gamma_e = 2.0$ injection spectrum. In the figures, we study what happens assuming the distribution of CRE's spectra follows a softer power-law behavior; in particular, we utilize spectra motivated by a recent analysis of Alpha-Magnetic Spectrometer results, indicating $\Gamma_e \sim 2.7$ [81], and by radio emission from synchrotron in the Galaxy [82], suggesting a harder CRE spectrum with $\Gamma_e \simeq 2.3$. We show results for the diffusion/source setups CRE3 and CRE4 in Fig. 7. While in the case of CRE3 softer injection spectra yield a slightly more centrally concentrated emission than for our $\Gamma_e = 2.0$ benchmark, in the case of CRE4 (where CREs are solely injected at the center) the effect of a change in the injection spectrum is very dramatic, with the CRE population, and thus the resulting IC signal, truncated at very small radii (around 2 kpc for $\Gamma_e - 2.7$ and 6 kpc for $\Gamma_e = 2.3$).

IV. PULSAR EMISSION

The pulsar population in M31 is modeled using the population synthesis code PsrPopPy [55]. In total, we generate 10,000 pulsars using default parameters for a Milky Way-type galaxy, appropriate in the present case. In particular, the radial distribution is based on the analysis of [83], while the vertical distribution assumes a two-sided exponential with scale height of $z_{\rm scale} = 0.33$ kpc. The pulsar spin period also is given in [83] as a log-normal distribution with $\mu = 2.7$ and standard deviation $\sigma = -0.34$. The total pulsar number was chosen as a reasonable estimate based on estimates from [84], where the theorized pulsar birth rate is estimated between 2.8

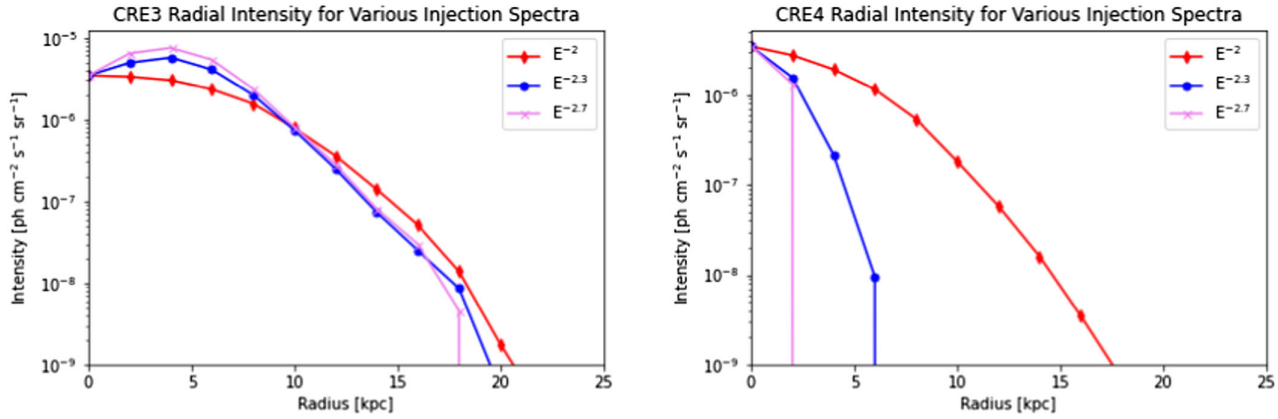

FIG. 7. Radial intensity profile for the diffusion/source setup CRE3 (left) and CRE4 (right) for three different injection spectra for the cosmic-ray electrons, $dN/dE_e \sim E^{-\Gamma_e}$, $\Gamma_e = 2$, 2.3, and 2.7.

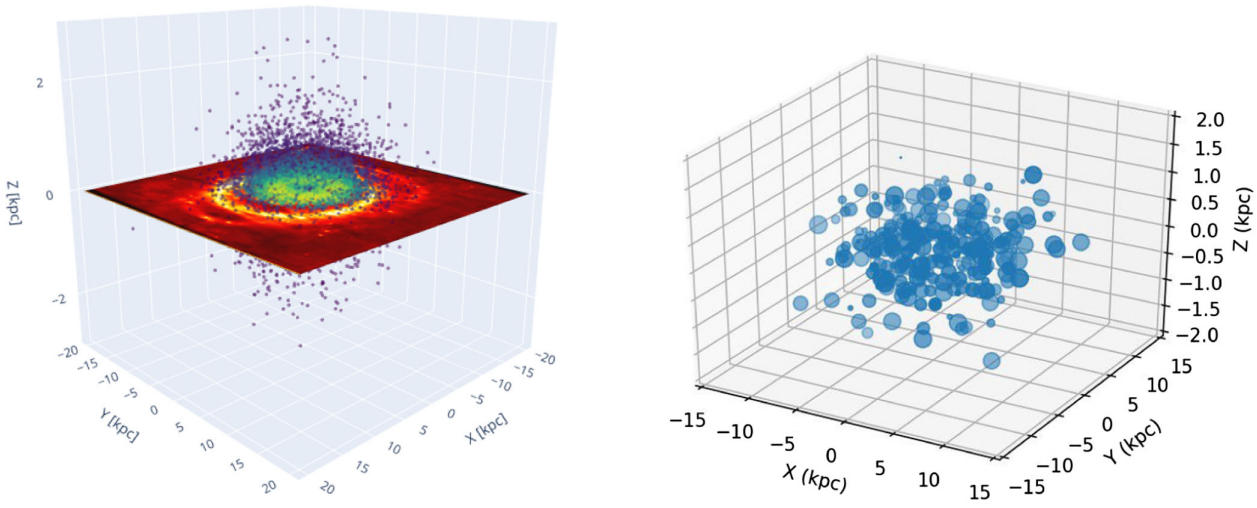

FIG. 8. Left: model pulsar population locations in relation to the galactic plane of M31. The colors of the pulsars are generated by a standard 3-D kernel density estimation. The plane image is the deprojected 24 μm image from Gordon *et al.* [54]. Right: example sample of 303 PWNe (enlarged by a factor 20).

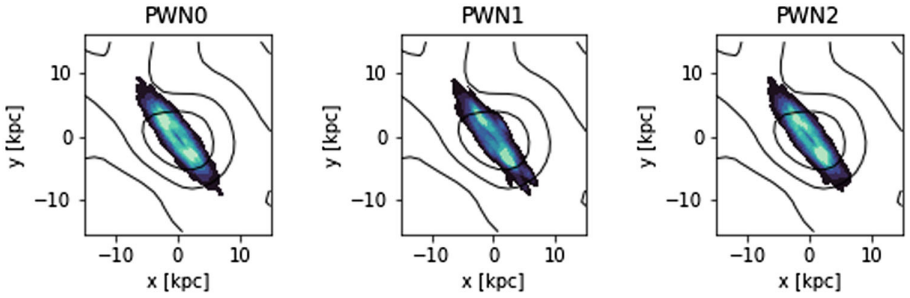

FIG. 9. The morphology of the gamma-ray emission from unresolved gamma-ray pulsars as predicted in the population synthesis model we constructed for the case where each pulsar features the same gamma-ray luminosity (PWN0) for $L_\gamma \propto \dot{E} \propto 1/(\tau P^2)$ (PWN1) and $L_\gamma \propto \sqrt{\dot{E}} \propto 1/(\sqrt{\tau} P)$ (PWN2).

pulsars per century, which would give a population of approximately 3000 pulsars and a larger possible number, which [84] suggests could be up to a factor 5 larger.

We sample the pulsar ages homogeneously and linearly between the ages of 10^3 yrs and 10^5 yrs, to bracket the observationally motivated age range of pulsars exhibiting a wind nebula (PWN) [85]. As far as the size of the PWN, we implement the functional dependence between age and radius of the nebula as in [58,85]. In Fig. 8, we show for illustrative purposes an image of the pulsar locations relative to the plane of the galaxy compared with a deprojected 24 μm image of M31 from [54]. Notice that in the figure we use different scales for the z axis and for the galactic plane. The right panel of Fig. 8 shows the size of the region of inefficient diffusion for a down selection of 303 random pulsars, enhanced for visibility by a factor 20 in size.

We utilize the synthetic population constructed as described above to simulate the sources of high-energy CRE in the case of CRE6, and we adopt for diffusion scenario (iii) again from CRE6 and for CRP6′ a suppressed diffusion coefficient 100 times smaller than in the rest of the diffusive cylindrical inner region. We also use the synthetic pulsar population to model a further possible (and plausible) source of gamma radiation.

As detailed in [86], the emission from gamma-ray pulsars is found to correlate with the pulsar's spin-down luminosity $\dot{E}$. Specifically, [86] finds that while several pulsars over a wide range of spin-down luminosities exhibit gamma-ray luminosities $L_\gamma \propto \dot{E}$ numerous others follow a phenomenological behavior where $L_\gamma \propto \sqrt{\dot{E}}$. Noting that the spin-down luminosity $\dot{E} \propto \dot{P}/P^3$, where P is the pulsar period and $\dot{P}$ the period derivative, and that the characteristic pulsar age $\tau = P/(2\dot{P})$, given our synthetic pulsar catalog, we simulated pulsar emission from the following two observationally motivated [86] prescriptions:

(1) $L_\gamma \propto \dot{E} \propto 1/(\tau P^2)$
(2) $L_\gamma \propto \sqrt{\dot{E}} \propto 1/(\sqrt{\tau} P)$

We also considered a model (0) where all pulsars produce the *same* gamma-ray emission. This latter case (0) can be considered a proxy for the emission from older, "recycled" millisecond pulsars, as considered, for instance, in [15] and in [14].

We show in Fig. 9 the expected gamma-ray emission from unresolved gamma-ray pulsars from the synthetic population we built as described above for the three cases PWN1 where $L_\gamma \propto \dot{E} \propto 1/(\tau P^2)$, PWN2 where $L_\gamma \propto \sqrt{\dot{E}} \propto 1/(\sqrt{\tau} P)$, and in the case PWN0 where the same gamma-ray luminosity is associated with every pulsar in the catalog. We observe a slight increase to the extension of the emission from PWN1 to PWN2 to the same-luminosity case. Overall, however, the pulsar emission appears to be relevant only for the innermost few kpc, as also reproduced in the detailed radial intensity profile shown in Fig. 10, where we normalize the emission to the inner galaxy data point, shown in red.

At their observed emission peaks of around 1 GeV, the gamma-ray luminosity of gamma-ray pulsars from the Fermi-LAT pulsar catalog [86] and millisecond pulsars

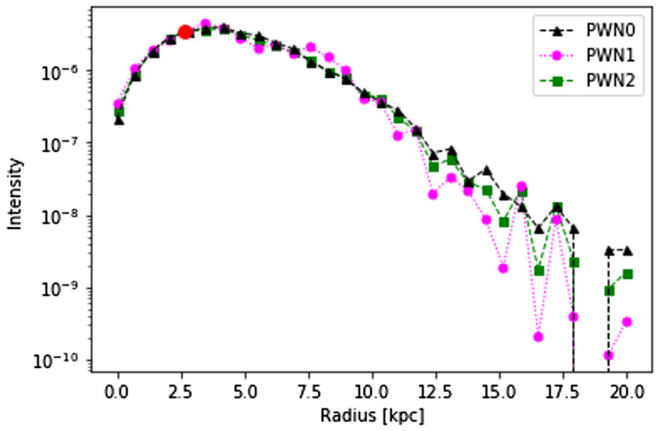

FIG. 10. The radial intensity profile, normalized to the measured gamma-ray intensity from the inner regions of M31, for the gamma-ray emission from unresolved gamma-ray pulsars as predicted in the population synthesis model we constructed for the case PWN0 of identical emission from each pulsar (black triangles) of $L_\gamma \propto \dot{E} \propto 1/(\tau P^2)$ (PWN1, purple circles) and $L_\gamma \propto \sqrt{\dot{E}} \propto 1/(\sqrt{\tau} P)$ (PWN2, green squares).

[see, e.g., [87]] is 10^{33}–10^{37} ergs s^{-1}. In order to account for 100% of the inner galaxy emission, the typical gamma-ray photon luminosity of each pulsar in our catalog would need to be around 4×10^{40} ph s^{-1}. For ∼1 GeV energies, this translates to a luminosity of 6.4×10^{37} ergs s^{-1}. Note that this does not take into consideration other sources of gamma-ray emission (e.g., star formation). Thus, while gamma-ray emitting pulsars alone are not sufficient to account for the total gamma-ray emission in Andromeda, based on both morphological arguments and energetics, we find that emission from unresolved gamma-ray pulsars in M31 is nevertheless likely to be a significant contributor in the inner regions of M31. In summary, based on both morphological arguments and energetics, we find that emission from unresolved gamma-ray pulsars in M31 is likely to be a significant contributor in the inner regions of M31.

V. DISCUSSION AND CONCLUSIONS

We studied the gamma-ray emission expected from the Andromeda galaxy (M31) due to high-energy cosmic-ray electrons and protons and by unresolved pulsar emission. The key motivation for the present study is the detection of gamma-ray emissions in the spherical halo and far outer halo of M31 [16] and the possibility that such emissions may be in part or entirely associated with a cosmic-ray "halo" extending significantly beyond the disk and bulge of M31.

We considered a broad ensemble of diffusion scenarios, including ones where diffusion is relatively efficient out to large radii and ones where diffusion is significantly inhomogeneous. We found that cosmic-ray electrons upscattering cosmic microwave background photons is likely responsible for a significant portion of the inner region gamma-ray emission and, possibly, of the spherical halo, especially if diffusion is highly inefficient near the sites of cosmic-ray electron acceleration. Cosmic-ray protons also definitely contribute to the inner-region emission and possibly to the emission in the outermost region, if the increase in the diffusion coefficient from the inner regions out to the virial radius is limited to within a factor of 5–10. Finally, we studied the possible contribution of unresolved pointlike sources associated with pulsars and found that this should only contribute to the inner region, with limited impact on the spherical halo emission.

We investigated the implications of the spectral information from the findings of Ackermann *et al.* [4]; at face value, we argued that this implies for a cosmic-ray proton scenario a spectrum $dN_p/dE_p \sim E_p^{-2.4}$ for a Dermer model and $dN_p/dE_p \sim E_p^{-2.3}$ for a fireball model. Assuming a Kolmogorov-type diffusion, this is consistent with what found in the Milky Way. In the case of cosmic-ray electrons, we showed how utilizing observationally motivated injection spectra, thus with a *softer* spectrum than our benchmark assumption, strongly focuses the predicted gamma-ray signal to the central regions of M31 and suppresses it at the periphery.

Our results provide further direct evidence for an extended cosmic-ray halo around M31 and thus possibly around our own Galaxy, as first entertained, for instance, in [17,18]. The simulations presented here suggest that diffusion-dominated CR transport is capable of driving CRs to large radii and could provide a significant contribution to gamma-ray emissions consistent with recent gamma-ray observations in the outer halo of M31 [16]. This analysis can further aid in our understanding of the properties of galactic halos. In particular, the presence of CRE at large radii is necessary for the production of large-scale synchrotron halos, which could provide a meaningful contribution to the observed radio background. Additionally, efficient CRE diffusion in quiescent galaxies such as M31 has been postulated as a significant factor in understanding the variety of galaxies that obey the radio-FIR correlation. This work explores and demonstrates that under reasonable CR injection and transport models the required CR halos can be realized while remaining consistent with the observational evidence from Fermi-LAT [16]. Nevertheless, while our results give some boundaries to their nature, the full composition of the halo in terms of its leptonic and hadronic components and the detailed structure of the diffusion configuration remain at present unclear. Given the possible new-physics interpretation of the gamma-ray emission from the outer regions of M31 [10], the cosmic-ray halo scenario should be carefully explored. Future observations both at gamma-ray and at other frequencies in conjunction with additional detailed cosmic-ray simulations and predictions at other wavelengths (including, e.g., radio and X-ray, where detailed data exist) will help further elucidate the origin of the gamma-ray emission from M31. For instance, [7] showed that the inner galaxy M31 gamma-ray emission can only be explained exclusively by cosmic-ray electrons as long as the magnetic field in the inner regions is highly suppressed compared to expected values in the several micro-Gauss range. Finally, given the similarities between M31 and the Milky Way, our results warrant establishing whether our own Galaxy possesses an extended cosmic-ray halo and, if so, how it would manifest observationally [see, e.g., [88]].

The data underlying this article will be shared on reasonable request to the corresponding author.

ACKNOWLEDGMENTS

S. P. is partly supported by the U.S. Department of Energy Grants No. DE-SC0010107 and No. A00-1465-001. We gratefully acknowledge early contributions by Henri Geneste, Lili Manzo, Lilianne Callahan, and helpful conversations with Tesla Jeltema.

[1] W. Atwood *et al.* (Fermi-LAT Collaboration), The Large Area Telescope on the Fermi gamma-ray space telescope mission, Astrophys. J. **697**, 1071 (2009).

[2] A. Abdo *et al.*, Fermi Large Area Telescope observations of Local Group galaxies: Detection of M 31 and search for M 33, Astron. Astrophys. **523**, L2 (2010).

[3] M. Pshirkov, V. Vasiliev, and K. Postnov, Evidence of Fermi bubbles around M31, Mon. Not. R. Astron. Soc. **459**, L76 (2016).

[4] M. Ackermann *et al.* (Fermi-LAT Collaboration), Observations of M31 and M33 with the Fermi Large Area Telescope: A galactic center excess in andromeda?, Astrophys. J. **836**, 208 (2017).

[5] M. Ajello, M. Di Mauro, V. Paliya, and S. Garrappa, The γ-ray emission of star-forming galaxies, Astrophys. J. **894**, 88 (2020).

[6] E. Storm, T. E. Jeltema, and S. Profumo, Gamma rays from star formation in clusters of galaxies, Astrophys. J. **755**, 117 (2012).

[7] A. McDaniel, T. Jeltema, and S. Profumo, Exploring a cosmic-ray origin of the multiwavelength emission in M31, Phys. Rev. D **100**, 023014 (2019).

[8] A. McDaniel, T. Jeltema, S. Profumo, and E. Storm, Multiwavelength analysis of dark matter annihilation and RX-DMFIT, J. Cosmol. Astropart. Phys. 09 (2017) 027.

[9] A. McDaniel, T. Jeltema, and S. Profumo, Multiwavelength analysis of annihilating dark matter as the origin of the gamma-ray emission from M31, Phys. Rev. D **97**, 103021 (2018).

[10] C. Karwin, S. Murgia, I. Moskalenko, S. Fillingham, A.-K. Burns, and M. Fieg, Dark matter interpretation of the Fermi-LAT observations toward the outer halo of M31, Phys. Rev. D **103**, 023027 (2021).

[11] M. Ackermann *et al.*, The Fermi Galactic Center GeV excess and implications for dark matter, Astrophys. J. **840**, 43 (2017).

[12] A. Albert *et al.*, Searching for dark matter annihilation in recently discovered Milky Way satellites with Fermi-LAT, Astrophys. J. **834**, 110 (2017).

[13] M. Ackermann *et al.*, Searching for Dark Matter Annihilation from Milky Way Dwarf Spheroidal Galaxies with Six Years of Fermi Large Area Telescope Data, Phys. Rev. Lett. **115**, 231301 (2015).

[14] G. Fragione, F. Antonini, and O. Y. Gnedin, Millisecond pulsars and the gamma-ray excess in Andromeda, Astrophys. J. Lett. **871**, L8 (2019).

[15] C. Eckner *et al.*, Millisecond pulsar origin of the Galactic Center Excess and extended gamma-ray emission from Andromeda - a closer look, Astrophys. J. **862**, 79 (2018).

[16] C. M. Karwin, S. Murgia, S. Campbell, and I. V. Moskalenko, Fermi-LAT observations of γ-ray emission toward the outer halo of M31, Astrophys. J. **880**, 95 (2019).

[17] R. Feldmann, D. Hooper, and N. Y. Gnedin, Circum-galactic gas and the isotropic gamma ray background, Astrophys. J. **763**, 21 (2013).

[18] M. Pshirkov, K. Postnov, and V. Vasiliev, Gamma-ray halo around the M31 galaxy as seen by the Fermi LAT, Proc. Sci., ICRC2015 (**2016**) 867.

[19] C. Evoli, P. Blasi, G. Morlino, and R. Aloisio, Origin of the Cosmic Ray Galactic Halo Driven by Advected Turbulence and Self-Generated Waves, Phys. Rev. Lett. **121**, 021102 (2018).

[20] T. Thomas, C. Pfrommer, and T. A. Enßlin, Probing cosmic ray transport with radio synchrotron harps in the Galactic Center, Astrophys. J. Lett. **890**, L18 (2020).

[21] T. Thomas and C. Pfrommer, Cosmic-ray hydrodynamics: Alfvén-wave regulated transport of cosmic rays, Mon. Not. R. Astron. Soc. **485**, 2977 (2019).

[22] T. Siegert, R. Diehl, G. Khachatryan, M. G. H. Krause, F. Guglielmetti, J. Greiner, A. W. Strong, and X. Zhang, Gamma-ray spectroscopy of positron annihilation in the Milky Way, Astron. Astrophys. **586**, A84 (2016).

[23] A. Abeysekara *et al.* (HAWC Collaboration), Extended gamma-ray sources around pulsars constrain the origin of the positron flux at Earth, Science **358**, 911 (2017).

[24] A. Strong and I. Moskalenko, Propagation of cosmic-ray nucleons in the galaxy, Astrophys. J. **509**, 212 (1998).

[25] B. C. Lacki, T. A. Thompson, and E. Quataert, The physics of the far-infrared-radio correlation. I. Calorimetry, conspiracy, and implications, Astrophys. J. **717**, 1 (2010).

[26] A. McCormick, S. Veilleux, and D. S. N. Rupke, Dusty winds: Extraplanar PAH features of nearby galaxies, Astrophys. J. **774**, 126 (2013).

[27] S. Veilleux, G. Cecil, and J. Bland-Hawthorn, Galactic winds, Annu. Rev. Astron. Astrophys. **43**, 769 (2005).

[28] J. Rossa and R. J. Dettmar, An Hα survey aiming at the detection of extraplanar diffuse ionized gas in halos of edge-on spiral galaxies. I. How common are gaseous halos among non-starburst galaxies?, Astron. Astrophys. **406**, 493 (2003).

[29] G. P. Ford *et al.*, Herschel exploitation of local galaxy Andromeda (HELGA). III. The star formation law in M31, Astrophys. J. **769**, 55 (2013).

[30] F. S. Tabatabaei and E. M. Berkhuijsen, Relating dust, gas, and the rate of star formation in M 31, Astron. Astrophys. **517**, A77 (2010).

[31] S. Rahmani, S. Lianou, and P. Barmby, Star formation laws in the Andromeda galaxy: Gas, stars, metals and the surface density of star formation, Mon. Not. R. Astron. Soc. **456**, 4128 (2016).

[32] E. M. Berkhuijsen, R. Beck, and F. S. Tabatabaei, How cosmic ray electron propagation affects radio-far-infrared correlations in M 31 and M 33, Mon. Not. R. Astron. Soc. **435**, 1598 (2013).

[33] D. D. Mulcahy, A. Fletcher, R. Beck, D. Mitra, and A. M. M. Scaife, Modelling the cosmic ray electron propagation in M 51, Astron. Astrophys. **592**, A123 (2016).

[34] M. Werhahn, C. Pfrommer, P. Girichidis, and G. Winner, Cosmic rays and non-thermal emission in simulated galaxies. II. γ-ray maps, spectra and the far infrared-γ-ray relation, Mon. Not. R. Astron. Soc. **505**, 3295 (2021).

[35] S. Colafrancesco, S. Profumo, and P. Ullio, Multi-frequency analysis of neutralino dark matter annihilations in the Coma cluster, Astron. Astrophys. **455**, 21 (2006).

[36] S. Colafrancesco, S. Profumo, and P. Ullio, Detecting dark matter WIMPs in the Draco dwarf: A multi-wavelength perspective, Phys. Rev. D **75**, 023513 (2007).

[37] M. Vollmann, Universal profiles for radio searches of dark matter in dwarf galaxies, J. Cosmol. Astropart. Phys. 04 (2021) 068.

[38] A. E. Vladimirov, S. W. Digel, G. Johannesson, P. F. Michelson, I. V. Moskalenko, P. L. Nolan, E. Orlando, T. A. Porter, and A. W. Strong, GALPROP WebRun: An internet-based service for calculating galactic cosmic ray propagation and associated photon emissions, Comput. Phys. Commun. **182**, 1156 (2011).
[39] C. Evoli, D. Gaggero, D. Grasso, and L. Maccione, Cosmic ray nuclei, antiprotons and gamma rays in the galaxy: A new diffusion model, J. Cosmol. Astropart. Phys. 10 (2008) 018.
[40] B. Tomasik, DRAGON: Monte Carlo generator of particle production from a fragmented fireball in ultrarelativistic nuclear collisions, Comput. Phys. Commun. **180**, 1642 (2009).
[41] L. Merten, J. Becker Tjus, H. Fichtner, B. Eichmann, and G. Sigl, CRPropa 3.1—A low energy extension based on stochastic differential equations, J. Cosmol. Astropart. Phys. 06 (2017) 046.
[42] R. Alves Batista *et al.*, CRPropa—A toolbox for cosmic ray simulations, J. Phys. Conf. Ser. **1181**, 012034 (2019).
[43] C. Gardiner, *Stochastic Methods: A Handbook for the Natural and Social Sciences*, 4th ed., Springer Series in Synergetics (Springer, New York, 2009).
[44] K. Fang, X.-J. Bi, S.-J. Lin, and Q. Yuan, Kleinnishina effect and the cosmic ray electron spectrum, Chin. Phys. Lett. **38**, 039801 (2021).
[45] J.-S. Niu and T. Li, Galactic cosmic-ray model in the light of AMS-02 nuclei data, Phys. Rev. D **97**, 023015 (2018).
[46] A. W. Strong, I. V. Moskalenko, and V. S. Ptuskin, Cosmic-ray propagation and interactions in the galaxy, Annu. Rev. Nucl. Sci. **57**, 285 (2007).
[47] R. Trotta, G. Jóhannesson, I. V. Moskalenko, T. A. Porter, R. Ruiz de Austri, and A. W. Strong, Constraints on cosmic-ray propagation models from a global Bayesian analysis, Astrophys. J. **729**, 106 (2011).
[48] S. E. Nuza, F. Parisi, C. Scannapieco, P. Richter, S. Gottlöber, and M. Steinmetz, The distribution of gas in the Local Group from constrained cosmological simulations: The case for Andromeda and the Milky Way galaxies, Mon. Not. R. Astron. Soc. **441**, 2593 (2014).
[49] R. Feldmann, D. Hooper, and N. Y. Gnedin, Circum-galactic gas and the isotropic gamma-ray background, Astrophys. J. **763**, 21 (2013).
[50] Z. Li, M. R. Garcia, W. R. Forman, C. Jones, R. P. Kraft, D. V. Lal, S. S. Murray, and Q. D. Wang, The murmur of the hidden monster: Chandra's decadal view of the supermassive black hole in M31, Astrophys. J. Lett. **728**, L10 (2011).
[51] E. Carlson and S. Profumo, When dark matter interacts with cosmic rays or interstellar matter: A morphological study, Phys. Rev. D **92**, 063003 (2015).
[52] E. Carlson, T. Linden, and S. Profumo, Cosmic-Ray Injection from Star-Forming Regions, Phys. Rev. Lett. **117**, 111101 (2016).
[53] E. Carlson, T. Linden, and S. Profumo, Improved cosmic-ray injection models and the Galactic Center gamma-ray excess, Phys. Rev. D **94**, 063504 (2016).
[54] K. D. Gordon *et al.*, Spitzer/mips infrared imaging of m31: Further evidence for a spiral-ring composite structure, Astrophys. J. **638**, L87 (2006).
[55] S. D. Bates, D. R. Lorimer, A. Rane, and J. Swiggum, PsrPopPy: An open-source package for pulsar population simulations, Mon. Not. R. Astron. Soc. **439**, 2893 (2014).
[56] D. Grasso *et al.* (Fermi-LAT Collaboration), On possible interpretations of the high energy electron-positron spectrum measured by the Fermi Large Area Telescope, Astropart. Phys. **32**, 140 (2009).
[57] S. Profumo, Dissecting cosmic-ray electron-positron data with Occam's Razor: The role of known Pulsars, Central Eur. J. Phys. **10**, 1 (2011).
[58] S. Profumo, J. Reynoso-Cordova, N. Kaaz, and M. Silverman, Lessons from HAWC pulsar wind nebulae observations: The diffusion constant is not a constant; pulsars remain the likeliest sources of the anomalous positron fraction; cosmic rays are trapped for long periods of time in pockets of inefficient diffusion, Phys. Rev. D **97**, 123008 (2018).
[59] H. Abdalla *et al.* (HESS Collaboration), The population of TeV pulsar wind nebulae in the H.E.S.S. Galactic Plane Survey, Astron. Astrophys. **612**, A2 (2018).
[60] D. J. Fixsen *et al.*, ARCADE 2 measurement of the absolute sky brightness at 3–90 GHz, Astrophys. J. **734**, 5 (2011).
[61] A. Kogut *et al.*, ARCADE 2 observations of galactic radio emission, Astrophys. J. **734**, 4 (2011).
[62] M. Seiffert *et al.*, Interpretation of the ARCADE 2 absolute sky brightness measurement, Astrophys. J. **734**, 6 (2011).
[63] J. J. Condon, W. D. Cotton, E. B. Fomalont, K. I. Kellermann, N. Miller, R. A. Perley, D. Scott, T. Vernstrom, and J. V. Wall, Resolving the radio source background: Deeper understanding through confusion, Astrophys. J. **758**, 23 (2012).
[64] N. Fornengo, R. A. Lineros, M. Regis, and M. Taoso, The isotropic radio background revisited, J. Cosmol. Astropart. Phys. 04 (2014) 008.
[65] G. Helou, B. T. Soifer, and M. Rowan-Robinson, Thermal infrared and nonthermal radio: Remarkable correlation in disks of galaxies, Astrophys. J. Lett. **298**, L7 (1985).
[66] G. Helou, I. R. Khan, L. Malek, and L. Boehmer, IRAS observations of galaxies in the Virgo cluster area, Astrophys. J. Suppl. Ser. **68**, 151 (1988).
[67] M. S. Yun, N. A. Reddy, and J. J. Condon, Radio properties of infrared-selected galaxies in the IRAS 2 Jy sample, Astrophys. J. **554**, 803 (2001).
[68] P. Hoernes, E. M. Berkhuijsen, and C. Xu, Radio-FIR correlations within M 31, Astron. Astrophys. **334**, 57 (1998).
[69] F. S. Tabatabaei, E. M. Berkhuijsen, P. Frick, R. Beck, and E. Schinnerer, Multi-scale radio-infrared correlations in M 31 and M 33: The role of magnetic fields and star formation, Astron. Astrophys. **557**, A129 (2013).
[70] E. de Cea del Pozo, D. F. Torres, and A. Y. Rodriguez Marrero, Multimessenger model for the starburst galaxy M82, Astrophys. J. **698**, 1054 (2009).
[71] U. Lisenfeld and H. J. Völk, On the radio spectral index of galaxies, Astron. Astrophys. **354**, 423 (2000).
[72] U. Lisenfeld, H. J. Völk, and C. Xu, The FIR/radio correlation in starburst galaxies: Constraints on starburst models, Astron. Astrophys. **314**, 745 (1996).
[73] B. Vollmer, M. Soida, R. Beck, and M. Powalka, Deciphering the radio star formation correlation on kpc scales.

I. Adaptive kernel smoothing experiments, Astron. Astrophys. **633**, A144 (2020).
[74] R. Beck, A. Brandenburg, D. Moss, A. Shukurov, and D. Sokoloff, Galactic magnetism: Recent developments and perspectives, Annu. Rev. Astron. Astrophys. **34**, 155 (1996).
[75] N. S. Kardashev, Nonstationarity of spectra of young sources of nonthermal radio emission, Sov. Astron. **6**, 317 (1962).
[76] F. S. Tabatabaei *et al.*, A detailed study of the radio-FIR correlation in NGC 6946 with Herschel-PACS/SPIRE from KINGFISH, Astron. Astrophys. **552**, A19 (2013).
[77] C. Pfrommer and T. A. Enßlin, Constraining the population of cosmic ray protons in cooling flow clusters with gamma-ray and radio observations: Are radio mini-halos of hadronic origin?, Astron. Astrophys. **426**, 777 (2004).
[78] C. D. Dermer, Secondary production of neutral pi-mesons and the diffuse galactic gamma radiation, Astron. Astrophys. **157**, 223 (1986).
[79] Q. An *et al.* (DAMPE Collaboration), Measurement of the cosmic-ray proton spectrum from 40 GeV to 100 TeV with the DAMPE satellite, Sci. Adv. **5**, eaax3793 (2019).
[80] K. Mannheim and R. Schlickeiser, Interactions of cosmic ray nuclei, Astron. Astrophys. **286**, 983 (1994).
[81] S. Zhao-Dong and L. Siming, Origin of cosmic ray electrons and positrons, Mon. Not. R. Astron. Soc. **485**, 3869 (2019).
[82] A. W. Strong, E. Orlando, and T. R. Jaffe, The interstellar cosmic-ray electron spectrum from synchrotron radiation and direct measurements, Astron. Astrophys. **534**, A54 (2011).
[83] D. R. Lorimer *et al.*, The Parkes Multibeam Pulsar Survey - VI. Discovery and timing of 142 pulsars and a Galactic population analysis, Mon. Not. R. Astron. Soc. **372**, 777 (2006).
[84] D. R. Lorimer, Radio pulsar statistics, in *Astrophysics and Space Science Library*, edited by W. Becker (Springer, Berlin, Heidelberg, 2009), Vol. 357, p. 1.
[85] H. Abdalla *et al.* (H. E. S. S. Collaboration), The population of TeV pulsar wind nebulae in the H.E.S.S. Galactic Plane Survey, Astron. Astrophys. **612**, A2 (2018).
[86] A. Abdo *et al.* (Fermi-LAT Collaboration), The second Fermi Large Area Telescope catalog of gamma-ray pulsars, Astrophys. J. Suppl. Ser. **208**, 17 (2013).
[87] D. Hooper and G. Mohlabeng, The gamma-ray luminosity function of millisecond pulsars and implications for the GeV excess, J. Cosmol. Astropart. Phys. 03 (2016) 049.
[88] L. Tibaldo *et al.*, Fermi-LAT observations of high- and intermediate-velocity clouds: Tracing cosmic rays in the halo of the Milky Way, Astrophys. J. **807**, 161 (2015).